Boron Nitride from Ammonia Borane and Alkali Amidoboranes and Its Features for Carbon Dioxide Capture

Carlos Castilla-Martinez, Rimeh Mighri, Christophe Charmette, Jim Cartier, Umit B. Demirci

Boron Nitride from Ammonia Borane and Alkali Amidoboranes and Its Features for Carbon Dioxide Capture

Carlos A. Castilla-Martinez,* Rimeh Mighri, Christophe Charmette, Jim Cartier, and Umit B. Demirci*

Herein, three boranes are studied as potential precursors of boron nitride (BN) and their carbon dioxide adsorption capacity is evaluated. The selected boranes are ammonia borane (AB, NH_3BH_3), lithium amidoborane (LiAB, $LiNH_2BH_3$), and sodium amidoborane (NaAB, $NaNH_2BH_3$), and they are pyrolyzed at four different temperatures. All the characterization techniques show the formation of BN from the three boranes. However, LiAB and NaAB form hexagonal BN (h-BN) at a lower temperature in comparison with AB. The insertion of the alkali metal inside the BN structure is also evidenced. These materials show interesting results when they are exposed to a CO_2 atmosphere. The materials are able to adsorb CO_2 at nearly ambient conditions, and the best results are achieved with samples that do not present a crystalline structure. AB treated at 600 °C uptakes 34 cm^3 g^{-1} (66.8 mg g^{-1}) at 1.5 bar CO_2 and 30 °C. Considering that the materials developed in this study are nonporous, the results are promising, opening new perspectives as potential sorbents for CO_2.

1. Introduction

Boron nitride (BN) is a versatile material that has been used in very different applications, such as medicine or energy.[1,2] Different precursors have been studied to obtain BN. Ammonia borane (AB) is a good example.[3,4] AB is a crystalline, stable solid at room temperature and under inert atmosphere, which has been widely studied for chemical hydrogen storage

due to its high hydrogen gravimetric density (19.6 wt%). During thermolysis, AB undergoes a three-step decomposition pathway, releasing 1 equivalent of H_2 in each stage. Each one of these steps takes place at about 100, 150, and >400 °C. Between 1200 and 1500 °C, crystalline hexagonal BN (h-BN) is obtained from AB.[4] Under the same logic, metal amidoboranes (MAB) might be considered as precursors of BN. MAB are derivatives of AB, where one of the protic hydrogens ($H^{\delta+}$) of the NH_3 moiety of the molecule has been substituted by a metal cation. These derivatives emerged due to some drawbacks presented by AB, such as the production of unwanted gaseous byproducts. MAB improved the dehydrogenation properties of pristine AB, as they start to release hydrogen at a lower temperature and they suppress some/all of the unwanted gaseous byproducts, delivering a purer H_2.[5] Up to now, different amidoboranes have been obtained experimentally: the family of alkali amidoboranes (Li, Na, K, Rb, Cs), some alkaline-earth amidoboranes (Mg, Ca, Sr, Ba), other MABs (e.g., Y-based), and the mixed cation amidoboranes (e.g., LiNa, NaAl).[6] MAB may offer some advantages as precursors of BN in comparison with AB[7–9]: 1) a lower temperature to obtain BN, as they start to dehydrogenate at lower temperatures; 2) a higher yield due to the emission of a lower quantity of gaseous byproducts (e.g., ammonia NH_3); 3) the metal cation could favor the crystallization of BN at lower temperatures; and 4) the alkali metal might be incorporated to the BN structure, giving tuned properties to the material.

As previously mentioned, BN has been used in a wide range of applications. One area that has been explored in recent years is the carbon dioxide capture. Limiting and reducing the concentration of CO_2 in the atmosphere is an urgent task. In this sense, BN appears as a potential material to capture CO_2 due to its properties. For example, through computational calculations, a strong adsorption between CO_2 and boron-rich BN nanotubes at ambient conditions was predicted (with a physisorption energy of 0.21 eV and a chemisorption energy of 0.82 eV).[10] Another theoretical study calculated the interaction between CO_2 and negatively charged BN nanosheets and nanotubes.[11] Uncharged BN structures weakly adsorbed CO_2; nevertheless, when the materials were negatively charged through the introduction of

C. A. Castilla-Martinez, R. Mighri, C. Charmette, J. Cartier, U. B. Demirci
Institut Européen des Membranes
IEM – UMR 5635, Université de Montpellier, ENSCM, CNRS
34090 Montpellier, France
E-mail: carlos.castilla-martinez@umontpellier.fr;
umit.demirci@umontpellier.fr

R. Mighri
Institut Charles Gerhardt Montpellier
ICGM – UMR 5253, Université de Montpellier
34090 Montpellier, France

The ORCID identification number(s) for the author(s) of this article can be found under https://doi.org/10.1002/ente.202201521.

**ADVANCED
SCIENCE NEWS**

www.advancedsciencenews.com

Energy Technology
Generation, Conversion, Storage, Distribution

www.entechnol.de

electrons, the BN structures were able to strongly adsorb the CO_2 molecules. The change in the adsorption energies from an uncharged BN structure to a negatively charged one was from 18.6 to 78.3 kJ mol^{-1} in the case of the nanosheets and from 15.8 to 66.9 kJ mol^{-1} for the nanotubes. Other computational studies have suggested different approaches to improve the gas sorption properties of BN, such as the increase of the specific surface area of the material or the functionalization with different metal atoms.[12,13] Some experimental studies have reported the adsorption of CO_2 by different BN structures. An early study from 1994 reported the use of porous BN for the selective CO_2 adsorption of a CH_4/CO_2 gas mixture.[14] More recently, different nanostructures such as nanofibers, nanosheets, 3D structures, or foams have been proposed for the capture of CO_2 at near ambient conditions.[15–21] A good example is a porous BN modified with a copolymer surfactant (P123).[17] With a specific surface area of 476 m^2 g^{-1}, this material was able to capture 60.2 cm^3 g^{-1} (or 118.3 mg g^{-1}) of CO_2 in 6 h, at 25 °C and under a constant flow of the gas (50 mL min^{-1}). Another example is pelletized porous BN fibers, with a specific surface area of 1098 m^2 g^{-1}.[21] The BN pellets were able to adsorb 50.6 cm^3 g^{-1} (or 99.4 mg g^{-1}) of CO_2 at 1 bar and 25 °C, showing also a selectivity of 20.6 for CO_2 over N_2.

In this context, we had two objectives in mind within the present study. The first one was to obtain BN structures using amidoboranes as precursors. We expected that the alkali metal present in these compounds would be inserted in the BN structure. Up to our knowledge, there is a lack of studies reporting the obtention of BN from amidoboranes. As a starting point, we selected two alkali derivatives of AB: the lithium (LiAB, $LiNH_2BH_3$) and sodium (NaAB, $NaNH_2BH_3$) amidoboranes. As a reference, we also used commercial AB. The samples were polymerized at 200 °C and then they were pyrolyzed at different temperatures (600, 800, and 1000 °C). We selected this range of temperatures to obtain samples with a high degree of dehydrogenation and to analyze the structures (amorphous/crystalline) obtained at these temperatures. Our second objective was to evaluate the materials as potential adsorbents of CO_2. The characterization and assessment of all the obtained compounds are described hereafter.

2. Results and Discussion

2.1. Preliminary Comments

The solids obtained by pyrolyzing AB, LiAB, and NaAB at 600 °C were analyzed by the N_2 adsorption technique. They are nonporous solids (Table S1, Supporting Information). At 800 °C, they showed a negligible specific surface area (SSA) (<10 m^2 g^{-1}). Thus, we consider that all the materials are nonporous. In addition, the pyrolyzed samples obtained from the alkali amidoboranes were analyzed by SEM. The images show a bulky structure of these samples (Figure S1, Supporting Information). The density of the materials was also measured (Table S1, Supporting Information), and the general trend is that when increasing the temperature, the density of the material also increases: AB goes from 1.3 × g cm^{-3} at 200 °C to 1.4 × g cm^{-3} at 1000 °C; LiAB from 1.0 to 2.0 × g cm^{-3} at the same temperatures; and

in the case of NaAB, from 1.5 to 1.7 × g cm^{-3}. As a reference, the density of pure h-BN is 2.1 × g cm^{-3}. We noticed that the density of AB and NaAB does not follow a constant trend when the temperature increases. At this point, the reason of this phenomenon is not clear and it needs a deeper investigation, but it is out of the scope of this study.

2.2. FTIR and ^{11}B MAS NMR

Commercial AB, the synthesized LiAB and NaAB, and the solids after pyrolysis were analyzed by FTIR. The spectra of AB, LiAB, and NaAB match well with the ones reported in the literature (Figure S2, Supporting Information).[6,22] The characteristic bands for the N—H and B—H stretching modes can be seen around 3000–3500 and 1800–2500 cm^{-1}, while the bending mode of the N—H and B—H bonds appears at around 1400–1600 and 1000–1300 cm^{-1} respectively. In the case of LiAB200 and NaAB200, the N—H and B—H stretching modes have almost disappeared, while for AB200 they are still visible; in addition, a strong peak at 1500 cm^{-1} appeared, revealing the presence of π bonded N and B atoms and indicating the formation of N-and B-based polymers BNH$_x$ ($x \leq 2$).[23] The AB200 FTIR spectrum also resembles the spectra of polyaminoborane, polyiminoborane, and polyborazylene.[24,25] When the temperature starts to increase (>600 °C), only two bands are visible. At 1000 °C, these two bands become more pronounced (**Figure 1**). As a reference, the spectrum of h-BN is shown.[26] The spectrum of AB1000 is similar to that of h-BN. Pristine h-BN shows two characteristics bands: one at about 1375 cm^{-1}, which is attributed to the B—N stretching vibration, and a second peak at about 815 cm^{-1}, corresponding to B—N—B bending vibrations. The LiAB1000 and NaAB1000 samples present similar spectra, which are also comparable to that of h-BN.

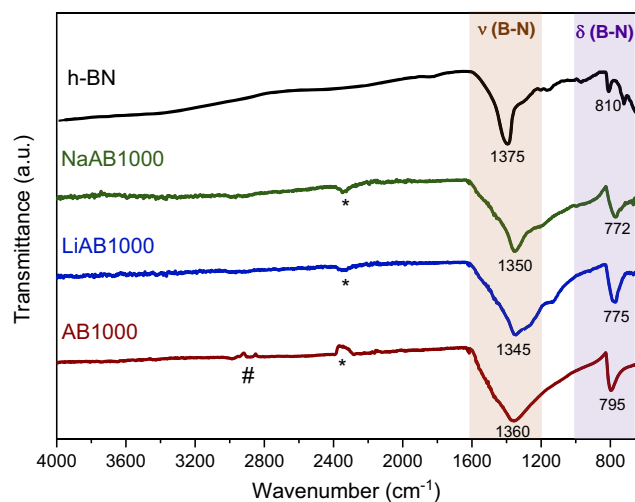**Figure 1.** Fourier-transform infrared spectroscopy (FTIR) spectra of ammonia borane (AB)100, lithium amidoborane (LiAB)100, sodium amidoborane (NaAB)100, and hexagonal boron nitride (h-BN). The star (*) indicates the presence of atmospheric CO_2 and the symbol (#) indicates the KBr film that protects the diamond of the FTIR apparatus. The vibrational modes in the colored rectangles and the wavenumbers in cm^{-1} are indicated.

ADVANCED
SCIENCE NEWS

www.advancedsciencenews.com

Energy Technology
Generation, Conversion, Storage, Distribution

www.entechnol.de

The difference in the wavenumbers between the vibrational bands of pure h-BN and those of the materials treated at 1000 °C is explained by the different degree of crystallinity of the samples and by the anisotropy of the h-BN structure.[4] The lattice vibrations are expected to be more pronounced in a crystalline material.

All the solids were analyzed by ^{11}B MAS NMR (Figure S3, Supporting Information). AB shows a single peak centered at −26 ppm, indicating a single NBH_3 environment. LiAB and NaAB show a single signal centered at −21 and −23 ppm, respectively, also indicating the NBH_3 environment.[27] When the temperature increases to 200 °C, new signals arise. In the negative chemical shifts, the signals are associated with different boron environments (BH_4 and N_2BH_2). In the case of AB200, the spectrum suggests the presence of different species, like the ion pair diammoniate of diborane (DADB) ($[H_3NBH_2NH_3]^+[BH_4]^-$) and polyaminoborane.[28–30] In the case of both LiAB200 and NaAB200, the signals that appear at negative chemical shifts are associated with DADB-like species, such as $[MNH_2BH_2MNH_2]^+[BH_4]^-$, or to coiled polymers such as $MNH_2BH_2LiNHBH_3$ (where M = Li, Na).[31] The formation of alkali borohydrides is also possible due to the signals associated to the BH_4 environment. For all the materials, a broad signal appeared in the trivalent boron area of the spectra (positive chemical shifts), which is associated with N_2BH and BN_3 environments, which suggest the formation of polyborazylene. At higher temperatures, this signal becomes the only one present in the spectra of the materials. At 1000 °C, the signal at positive chemical shifts broadens and it becomes more symmetrical (**Figure 2**). The spectra of AB1000, LiAB1000, and NaAB1000 resemble to the spectrum of BN.[32] As the temperature of the heat treatment is high (>600 °C), most of the hydrogen from the borane molecules should have been released, and a major presence of BN_3 species is expected. Both FTIR and MAS NMR analyses indicate the successful synthesis of pristine LiAB and NaAB, and the formation of BN from AB, LiAB, and NaAB at high temperatures.
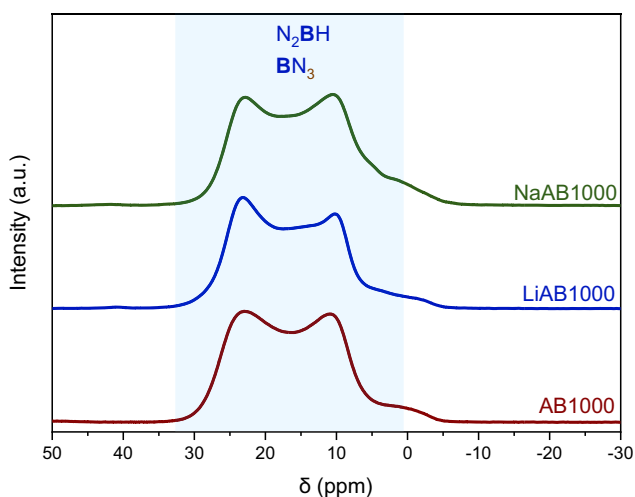

Figure 2. ^{11}B magic-angle spinning nuclear magnetic resonance (MAS NMR) spectra of AB and the alkali amidoboranes pyrolyzed at 1000 °C. The chemical environments have been assigned in the colored rectangle.

2.3. Raman Spectroscopy

The materials obtained after the pyrolysis of AB, LiAB, and NaAB were analyzed by Raman spectroscopy. AB200 presents three broad bands at 3440, 2510, and 1400 cm^{-1} (**Figure 3**a). The bands at 3440 and 2510 cm^{-1} indicate the presence of N—H and B—H groups that are bonded to a single H atom, which suggests the formation of polyborazylene, in agreement with the MAS NMR results.[33] The broad band at 1400 cm^{-1} is attributed to the stretching mode of the B—N bond. The bands below 1250 cm^{-1} correspond to the bending modes of N—H and B—H groups, indicating an incomplete dehydrogenation of the material. Some of these signals are still observed for AB600, indicated by a star in the figure. At 800 and 1000 °C, all the bands have disappeared and a broadband starts to form around 1370 cm^{-1}. This signal is associated to the stretch of the B—N graphitic-layered structure of h-BN (the E_{2g} vibrational mode).

The spectrum of LiAB200 (Figure 3b) shows a signal at 2287 cm^{-1}, which corresponds to the B—H stretching mode. As this band is broad and small, it indicates the dehydrogenation of the BH_3 group to BH species. Another broadband can be seen at 1337 cm^{-1}, comparable to the stretching B—N vibrational mode in BN. Similar to the lithium-based sample, NaAB200 (Figure 3c) presents some low-intense peaks at 2280 cm^{-1}; in addition, an extra peak at 1100 cm^{-1} is observed that is associated to the deformations of NH_2 and BH_3 fragments of the polymers (wagging, rocking, bending movements).[34] LiAB600 and NaAB600 show a single peak in the stretching region associated to h-BN. The peak becomes sharper and more intense as the temperature increases. In 1981, Nemanich established a relation between the Raman spectrum of BN and the crystal grain size through the width broadening (full width at half-maximum [FWHM]) of the peak and the energy of the E_{2g} mode.[35] Ergo, when the E_{2g} vibrational mode shifts to a higher frequency and the peak broadens, the average crystal size of BN decreases. This relation has been reported for different BN nanostructures.[36,37]

On the one hand, the E_{2g} mode of the AB-derived materials appears as a broad band, suggesting the formation of a disordered BN. On the other hand, this signal appears as a sharp peak for the samples derived from the amidoboranes from 600 °C. Through the relation given by Nemanich, the average crystal grain size of the BN was calculated (Table S2, Supporting Information). In our case, the FWHM of the materials decreases as the temperature is increased and thus, the grain size of the crystals is increased. Through this method, an average grain size of 9.5 and 7.2 nm was calculated for LiAB1000 and NaAB1000, respectively. The Raman analyses showed that BN is formed by the pyrolysis of LiAB and NaAB, and this BN achieved a higher degree of crystallinity in comparison with the one obtained from AB. This is related to the role of the metal cation (Li$^+$, Na$^+$), as suggested elsewhere.[38]

2.4. PXRD

All the samples were analyzed by PXRD (**Figure 4**). The diffraction pattern of AB is presented in the Figure 4a. It matches well with the ones reported in the literature and it corresponds to a
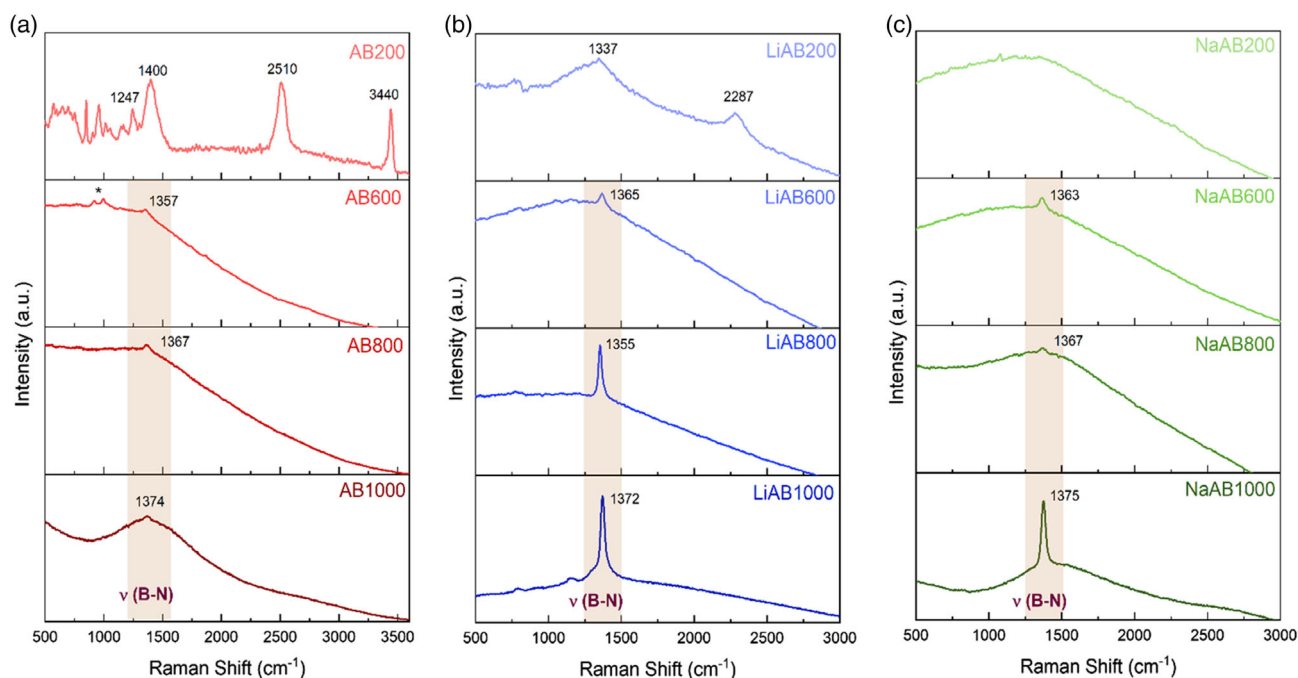
Figure 3. Raman spectra of the pyrolysis products at 200, 600, 800, and 1000 °C for a) AB, b) LiAB, and c) NaAB. The vibrational bands of interest and the Raman shifts in cm^{-1} are indicated. The star (*) indicates the incomplete dehydrogenation of AB at 600 °C.
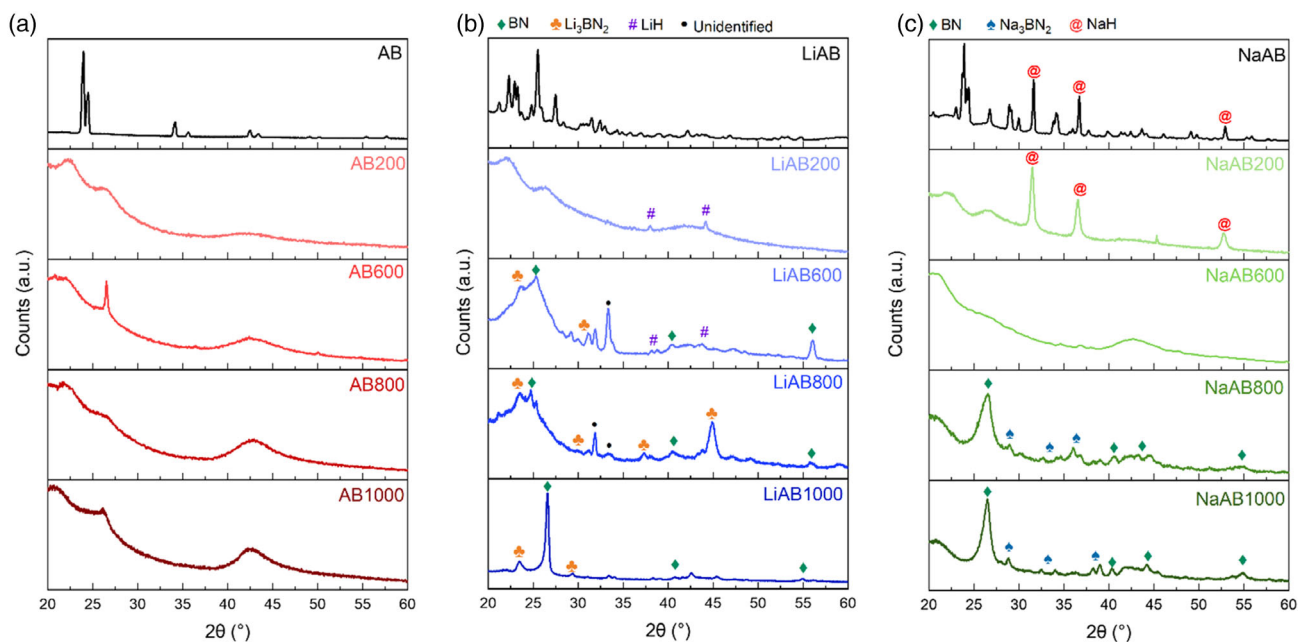

Figure 4. Powder X-ray diffraction (PXRD) patterns of the pristine boranes and their solid products obtained after heat treatment at 200, 600, 800, and 1000 °C: a) AB, b) LiAB, and c) NaAB. The identified byproducts are indicated by the colored figures.

body-centered tetragonal structure, with a I4 mm space group.[39] AB200 is an amorphous solid, suggesting the presence of polymeric species such as polyaminoborane and polyborazylene. As the temperature increases, two broad signals start to appear around 26° and 42° and the intensity of the signals increase. The relatively low intensity and the broadness of the signals at 26° and 42° indicate the formation of thin BN layers with a weak stacking and a poor crystallinity.[40] It is possible that a turbostratic BN (t-BN) structure starts to form, which is characterized by graphitic layers with a random orientation, and can be seen as an intermediate between amorphous BN and h-BN.[41,42]

LiAB presents two allotropes, with an orthorhombic unit cell and *Pbca* space group: α-LiAB and β-LiAB, where the lattice parameters of the β-phase are almost twice the ones of the α-phase.[43] The pattern presented in the Figure 4b corresponds to β-LiAB, which is formed under energetic ball milling. LiAB200 is an amorphous solid, with no traces of the original diffraction peaks of the former LiAB. Two peaks can be seen in the diffractogram, which belong to LiH (ICSD CollCode 173177), and they are still present for the LiAB600 sample, but with a lower intensity. Some of the additional peaks were identified. For example, Li_3BN_2 (ICSD CollCode 41022) was detected. The presence of this compound is explained by the formation of Li_2NH between 300 and 450 °C. Li_2NH decomposes into metallic Li, H_2, and N around 750 °C.[44] Some of the metallic Li could react with gaseous N_2 to form Li_3N, which in turn would further interact with the BN-like structures to form Li_3BN_2.[7] LiAB1000 presents the characteristic peaks of h-BN (ICSD CollCode 240996) at 26°, 41°, 44°, and 55°.

The diffraction pattern of NaAB matches well with the patterns reported in the literature (Figure 4c); however, some diffraction peaks belonging to NaH (ICSD CollCode 33670) can be observed. The presence of unreacted NaH alongside with NaAB is a recurrent problem in the synthesis of this amidoborane by ball milling.[45] NaAB200 and NaAB600 are amorphous solids. At 800 °C, the sample starts to show some diffraction peaks. NaAB1000 clearly shows the characteristic peaks of h-BN and some other peaks which have been attributed to Na_3BN_2 (ICSD CollCode 68619). To explain the presence of Na_3BN_2, we considered the formation of amorphous $NaBH_4$ (which was suggested by the ^{11}B MAS NMR results). $NaBH_4$ can react with $NaNH_2$ to form Na_2BNH_6, which dehydrogenates above 600 °C, producing Na_3BN_2. The latter slowly decomposes, producing metallic Na, N_2, and BN in the 680–1100 °C range.[46]

From Figure 4, it is clear that crystalline h-BN is formed from 600 °C for LiAB and from 800 °C for NaAB. The crystallinity of the sample increases when the temperature rises, as the diffraction peaks are sharper and more intense. In concordance with the Raman analyses, we confirm the formation of h-BN from both alkali amidoboranes. It is likely that the metal cations (Li^+ and Na^+) play a role in the crystallization of h-BN, as they showed a higher degree of crystallinity at lower temperatures in comparison with pristine AB.[7,38]

LiAB1000 and NaAB1000 were analyzed by HR-TEM (Figure S4, Supporting Information). The interlayer lattice for LiAB1000 and NaAB1000 was estimated as 0.335 and 0.337 nm, which is in good agreement with the theoretical value of a well crystallized BN (0.333 nm),[7] and confirmed the high crystallization degree showed by the PXRD analysis.

2.5. XPS

The solids obtained after the pyrolysis of AB were analyzed by XPS for B 1*s* (**Figure 5**a). The spectra were deconvoluted into two signals. For AB200, the signal at 190.2 eV is attributed to the B—N bond. This peak is present in all the materials, and it shifts to higher energies (i.e., from 190.2 to 190.5 eV) as the temperature raises. This is an evidence of the formation of a BN structure, which starts to show a higher layer arrangement when the temperature increases, in agreement with the PXRD analyses.[47,48] The second peak is assigned to $B_xN_yO_z$, which indicates that an oxygen atom has substituted a nitrogen atom in the BN structure.[49,50] The binding energy of the peak depends on the atoms bonded to the boron atom (i.e., NBO_2 or N_2BO).[51,52] It is still unclear if the oxygen comes from an oxidation of the sample when it briefly enters in contact with air before the pyrolysis, from an oxygen pollution of the N_2
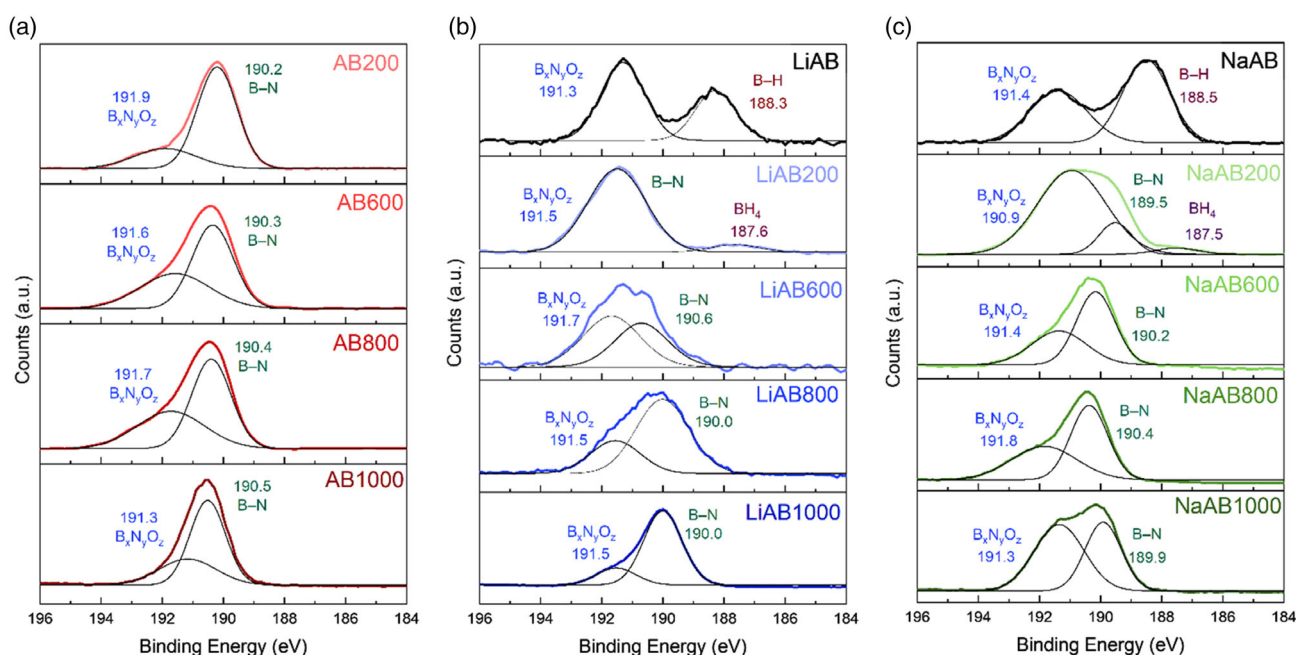

Figure 5. B 1*s* X-ray photoelectron spectroscopy (XPS) spectra of a) the pyrolysis products of AB, b) LiAB, and c) NaAB (and their pyrolysis products). The binding energies in eV and the associated bonds are indicated. The component bands were deconvoluted using a Gaussian fit.

**ADVANCED
SCIENCE NEWS**

www.advancedsciencenews.com

Energy Technology
Generation, Conversion, Storage, Distribution

www.entechnol.de

stream in the furnace, or before the XPS analysis due to the handling of the samples under air.

The spectra of pristine LiAB and NaAB were deconvoluted in two peaks (Figure 5b,c). The peak centered at 188 eV is assigned to the B—H bonds of the BH_3 moiety of the molecules.[53] The peak that appears at 191 eV suggests the partial hydrolysis of the BH_3 group of the amidoboranes, which are highly sensitive compounds to air and moisture.[6] It is probable that this occurred during the handling of the samples before the XPS analysis, which are prepared under air. The spectra of LiAB200 and NaAB200 present some changes: there is a signal that appears at 187 eV, suggesting the presence of BH_4-containing species, like DADB-like structures, $NaBH_4$ or $LiBH_4$.[54] This is in good agreement with the ^{11}B MAS NMR spectra of these compounds (Figure S3, Supporting Information). The absence of diffraction peaks belonging to the MBH_4 (M = Li, Na) in the PXRD diffractograms (Figure 4) indicates that they might be present in an amorphous form. The spectrum of LiAB200 shows a broad signal at 191.5 eV, which belongs to $B_xN_yO_z$ and that indicates a rapid oxidation under air. It is likely that this broad signal overlaps the expected B—N signal at $\approx$190 eV. The spectra of both amidoboranes treated at 600, 800, and 1000 °C were deconvoluted into two main signals. As in the case of AB, the signal that appears at 190 eV is attributed to the B—N bond in BN structures. In addition, all the samples presented the $B_xN_yO_z$ signal centered at $\approx$191 eV, indicating the presence of oxygen atoms in the BN structure.

Regarding the N1s spectra of the solids obtained after the pyrolysis of AB, all the curves were deconvoluted into two signals (Figure S5, Supporting Information). The signal that appears at $\approx$398 eV corresponds to the N—B bond in polyborazylene-like species in the case of AB200; for the rest of the samples, it is attributed to the N—B bond in BN.[47] The other signal centered at $\approx$398.8 eV is attributed to the $B_xN_yO_z$ species. In the case of the pristine amidoboranes, the spectra showed a single signal centered at $\approx$399.5 eV belonging to N—H bonds. However, we do not discard a possible contribution from the N—M bond to this signal.[55] After pyrolysis, the spectra were deconvoluted into mainly two peaks centered at 397.8 eV ($\pm$0.3 eV) and at $\approx$398.9

($\pm$0.3) eV for both amidoboranes. The first one is assigned to the N—B bond in BN and the second to the $B_xN_yO_z$.

The XPS analyses also confirmed that BN is formed through the thermolysis of AB, LiAB, and NaAB. In addition, the presence of $B_xN_yO_z$ was identified systematically for all the samples, indicating that oxygen atoms are incorporated to the structures, either due to a contact with air during the pyrolysis process, and/or before the XPS analysis. It has been reported that the presence of oxygen into the BN structure might enhance the gas (H_2) sorption properties of BN.[56,57] Nevertheless, to make a comparison between O-doped BN and pure BN seems to be complicated, as a completely oxygen-free BN is required.

2.6. The Alkali Elements

To have a better understanding on the evolution of the alkali elements of LiAB and NaAB after each heat treatment, all the pyrolyzed solids were analyzed by MAS NMR and XPS. The ^7Li MAS NMR spectra for LiAB and its pyrolysis products are shown in **Figure 6**a. LiAB shows a single broad single centered at 2.3 ppm that is assigned to the **Li**—NH_2BH_3 environment. In the case of LiAB200, the signal shifted to 0.1 ppm. This shift is explained by the release of hydrogen from the sample, which leads to the reduction of the electronegativity on the N atom and thus, electron density of the Li atom increases.[58] The samples LiAB600, LiAB800, and LiAB1000 show again a band centered at 2.2 ppm, which is attributed to a BN-like structure with tentative formula Li—NBH_x ($x \leq 2$, depending on the temperature). This signal suggests the insertion of some Li atoms into the BN structure. Additionally, LiAB800 presents two more environments at -0.3 and -5.5 ppm. The first is attributed to a dehydrogenated form of LiH.[59] For the second, there is no conclusive identification of this band. It might belong to the Li_3BN_2, identified by PXRD, or by some residues of another byproduct from the LiAB pyrolysis.

NaAB and its pyrolyzed products were characterized by ^{23}Na MAS NMR spectroscopy (Figure 6b). A signal at $\approx$18 ppm is present in all the samples. This signal is due to the presence of NaH.[60] As shown by the PXRD analysis, unreacted NaH was present alongside the pristine NaAB. As the temperature
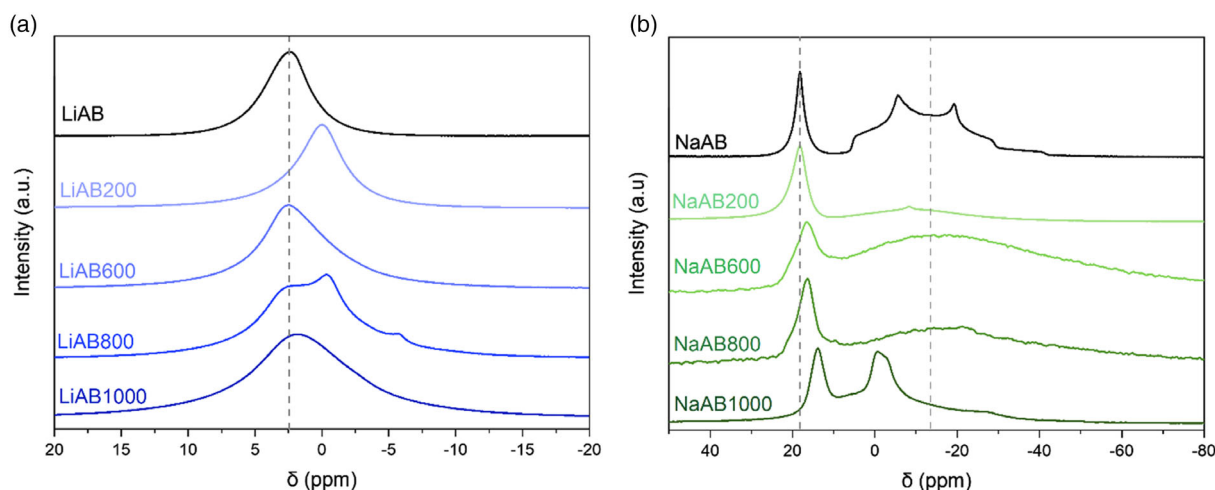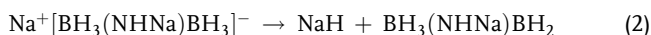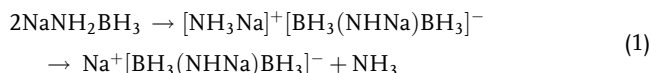

Figure 6. a) ^7Li and b) ^{23}Na MAS NMR spectra for LiAB, NaAB, and their respective pyrolysis products at 200, 600, 800, and 1000 °C.

ADVANCED
SCIENCE NEWS

www.advancedsciencenews.com

Energy Technology
Generation, Conversion, Storage, Distribution

www.entechnol.de

increases, this band shifts toward smaller δ values. This might indicate the dehydrogenation of the species, as in the case of LiH. In addition, new NaH might form due to the decomposition mechanism of NaAB, following the reactions[61]

$$2NaNH_2BH_3 \rightarrow [NH_3Na]^+[BH_3(NHNa)BH_3]^- \\ \rightarrow Na^+[BH_3(NHNa)BH_3]^- + NH_3 \tag{1}$$

$$Na^+[BH_3(NHNa)BH_3]^- \rightarrow NaH + BH_3(NHNa)BH_2 \tag{2}$$

Pristine NaAB shows a band with a large quadrupolar interaction centered at -13 ppm, due to the **Na**—NH_2BH_3 environment.[62] This signal starts to decrease in intensity and to broaden when the temperature is increased, due to the dehydrogenation and amorphization of the sample. NaAB800 presents a sharp peak at 1130 ppm (Figure S6, Supporting Information), which indicates the formation of metallic sodium due to the decomposition of NaH.[62] This high difference in the chemical displacement is explained by the Knight shift, which occurs when there are two different environments present in the sample (a pure metallic environment and a nonmetallic one). Finally, a new environment can be seen in the spectrum of NaAB1000 at -1.5 ppm, which suggests a Na site in a BN-like structure.

The Li 1s and Na 1s XPS spectra for LiAB, NaAB, and their pyrolysis products are presented in **Figure 7**. LiAB presents a symmetrical signal centered at 55.0 eV, which is assigned to the Li—N bond. For comparison, a binding energy of 55.2 eV was reported for LiN_3.[55] This signal appears at every temperature, indicating that the Li—N bond is still present even at 1000 °C, confirming the insertion of the Li into the BN structure. LiAB1000 shows another small signal at 56.4 eV, attributed to Li_2O, which can be formed due to the oxidation of a small quantity of metallic Li formed during the pyrolysis. We do not discard

a contribution from the Li_3BN_2 to this signal, identified by PXRD. The spectrum of pristine NaAB shows a single symmetrical band at 1071.3 eV, assigned to the Na—N bond. As for LiAB, this signal is present in all the samples. Also similar to LiAB, the NaAB600 and NaAB800 present a second band centered at $\approx$1073 eV that indicates the oxidation of metallic Na.[55]

The MAS NMR and XPS analyses confirm the presence of oxidized species, present due to the oxidation of the as-formed pure alkali metal (Li, Na) when it enters in contact with the air. The analyses were also useful to confirm that the alkali metal was inserted in the BN structure, which would give to these materials different properties in comparison with pristine BN.

2.7. CO_2 Sorption Experiments

The CO_2 capture capacity of the pyrolyzed samples was investigated. Each sample was exposed to a CO_2 atmosphere of 1.5 bar and the variation of the pressure with respect to the time was measured. The sorption capacity of the samples is shown in **Table 1**.

None of the materials treated at 200 °C were able to adsorb CO_2. As previously discussed, the samples are formed by a mixture of different boron- and nitrogen-based polymers at this temperature (e.g., polyaminoborane, polyborazylene). It is likely that the structure of these inorganic polymers hinders the adsorption of CO_2. The case of the amidoborane-based materials is similar (with exception of the NaAB600). These materials did not uptake CO_2, which might be related to their structure. This will be discussed later.

The samples of AB and NaAB treated at 600 °C were able to uptake CO_2. The CO_2 adsorbed by AB600, which presented the maximum capacity reached in this study, is 34 cm^3 g^{-1}
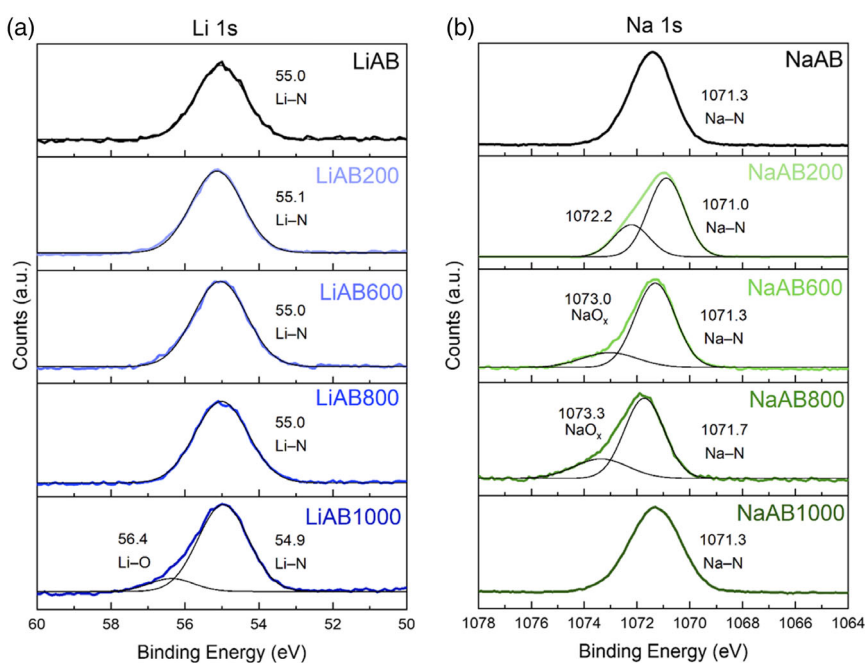

Figure 7. XPS spectra of the amidoboranes and the solid product after pyrolysis at 200, 600, 800, and 1000 °C of a) Li 1s for LiAB and b) Na 1s for NaAB. The binding energies in eV and the associated bonds are indicated.

ADVANCED
SCIENCE NEWS
www.advancedsciencenews.com

Energy Technology
Generation, Conversion, Storage, Distribution
www.entechnol.de

Table 1. CO_2 adsorption capacities of the materials obtained in this study.

Material	T [°C]	P [bar]	CO_2 uptake [cm^3 g^{-1}]	[mg g^{-1}]
AB200	30	1.5	–	–
AB600	30	1.5	34	66.8
AB800	30	1.5	32.7	64.3
AB1000	30	1.5	21.9	43
LiAB200	30	1.5	–	–
LiAB600	30	1.5	–	–
LiAB800	30	1.5	–	–
LiAB1000	30	1.5	–	–
NaAB200	30	1.5	–	–
NaAB600	30	1.5	17.7	34.9
NaAB800	30	1.5	–	–
NaAB1000	30	1.5	–	–

(66.8 mg g^{-1}); and the CO_2 absorbed by NaAB600 is 17.7 cm^3 g^{-1} (34.9 mg g^{-1}). Interestingly, at 800 °C, the CO_2 capture capacity of AB800 is slightly reduced (32.7 cm^3 g^{-1} or 64.3 mg g^{-1}), while the capacity of NaAB800 could not be measured either. The CO_2 uptake capacity of AB1000 is reduced to 21.9 cm^3 g^{-1} (43 mg g^{-1}). The samples that were able to adsorb CO_2 were analyzed by thermogravimetric analysis (TGA) right after the sorption experiments. According to Table 1, the CO_2 adsorbed by AB600, AB800, and NaAB800 is 6.7, 6.4, and 3.5 wt%. During the TGA analysis, AB600 and NaAB600 lost 1.5 and 2.3 wt% up to 200 °C and AB800 did not show any mass loss up to this temperature. These results suggest that the CO_2 is weakly adsorbed by the materials and in equilibrium and once the CO_2 atmosphere is removed, all or most of the CO_2 is desorbed.

At this point, it is possible to make a relation between the adsorption of CO_2 and the degree of crystallization of the samples. The samples AB600, AB800, AB1000, and NaAB600 were able to adsorb CO_2; AB600 showed the best result of this study. The PXRD results (Figure 4) showed that these four samples present an amorphous structure. It is likely that they are formed mostly of amorphous BN, but it is also possible that a turbostratic structure has started to form in some of these materials. t-BN presents impurities, incomplete bonds, a random orientation of the layers, and vacancies.[41] All of these defects in the structure would confer a high number of potential sites for the capture of CO_2. As also discussed in Section 3.4, the samples derived from LiAB showed diffraction peaks from 600 °C, while the NaAB-derived materials did from 800 °C. This would explain why the materials obtained from LiAB did not adsorb CO_2 (they presented a higher degree of crystallinity); while the only Na-based material that was able to uptake CO_2 is NaAB600 (NaAB600 is amorphous while NaAB800 presents diffraction peaks associated to h-BN). In addition, the materials derived from AB showed no crystallinity and they presented the best values in terms of adsorption. The highest adsorption value was achieved by AB600 and then it started to decrease, as the temperature of the treatment increased. With the raise of the temperature, the BN layers in AB800 and AB1000 should be more ordered, which coincides with the reduction on the CO_2 adsorption.

It is also worth mentioning that the adsorption of CO_2 presented by all the materials are higher than the reported for pristine h-BN (1.7 cm^3 g^{-1} or 3.3 mg g^{-1}) (**Table 2**).[19] The results from the samples AB600, AB800, and NaAB600 are promising, as these materials are nonporous. They showed better results than some other nanostructured materials based on BN (Table 2). The development of porous materials based on these three samples is desirable, to increase their sorption capacity.

3. Conclusions

AB and two of its alkali derivatives, LiAB and NaAB, were used as precursors of BN. The synthesis, pyrolysis, and characterization of these materials were carried out. Through this study, we show the successful synthesis of h-BN from both amidoboranes. At 200 °C, the materials are composed of amorphous polymers based on boron and nitrogen. At 600 °C, the LiAB-derived sample already shows the presence of crystalline h-BN, evidenced by the PXRD and Raman spectroscopy techniques. The formation of h-BN is also evidenced for NaAB when it is treated at 800 °C. In the case of AB, it does not show a crystalline structure, even when

Table 2. CO_2 uptake by different BN-based materials.

Material	T [°C]	P [bar]	SSA [m^2 g^{-1}]	CO_2 uptake [cm^3 g^{-1}]	[mg g^{-1}]	Reference
AB600	30	1.5	–	34	66.8	This work
AB800	30	1.5	–	32.7	64.3	
NaAB600	30	1.5	–	17.7	34.9	
Sphere functionalized BN nanosheets/ZnO	25	1	71.2	40	78.6	[16]
Cubic functionalized BN nanosheets/ZnO	25	1	25.1	16.6	32.6	[16]
Pristine porous BN	25	1	102	44.8	88	[17]
P123-modified porous BN	25	1	476	60.2	118.3	[17]
3D flower-like BN nanosheets	25	1	1114	19.2	37.7	[19]
Pristine h-BN	25	1	–	1.7	3.3	[19]
BN nanosheets	25	1	235	10	19.6	[20]
Pelletized porous BN fibers	25	1	1098.9	50.6	99.4	[21]

treated up to 1000 °C. With the aid of all the characterization techniques, we conclude that amidoboranes are precursors of h-BN. In addition, the alkali cation plays a role in the crystallization process, as LiAB and NaAB led to h-BN at a lower temperature in comparison with AB. Thus, alkali amidoboranes can be considered as a viable source to obtain crystalline BN from 600 to 800 °C. We also confirmed the insertion of the alkali metal in the BN structure.

The pyrolyzed solids obtained from AB, LiAB, and NaAB were also studied as potential materials for CO_2 capture. The adsorption experiments showed that these materials are able to capture CO_2 at nearly room conditions (1.5 bar CO_2 and 30 °C). The sample derived from AB treated at 600 °C presents the best results ($34 \, cm^3 \, g^{-1}$ or $66.8 \, mg \, g^{-1}$), while the samples derived from LiAB and NaAB show a poor performance (with the exception of NaAB600). It is likely that this is related to the crystallinity degree of the samples. It is also probable that AB600 presents a high amount of defects in the structure, which favor the adsorption of CO_2. On the contrary, LiAB-derived samples show a higher degree of crystallinity and thus, a lower capture capacity. The samples that were able to adsorb CO_2 present higher values than the one reported for pristine h-BN. The materials obtained in this work are nonporous and thus, the results are promising. However, the materials desorbed all or most of the CO_2 once the gas atmosphere was removed. To improve these results, it would be necessary to obtain a porous material based on AB pyrolyzed at 600 °C, which showed the best performance. The selectivity of the materials for CO_2 over a mixture of gases needs to be evaluated too. Studies are in progress to analyze these aspects.
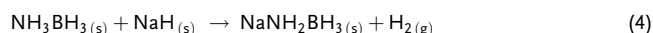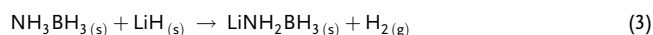
4. Experimental Section

Reagents: The reagents used for this study were AB (Sigma Aldrich, 97%), lithium hydride LiH (Sigma Aldrich, 95%), and sodium hydride NaH (Sigma Aldrich, dry, 90%), which were used as received. All the reagents were stored in an argon-filled glove box (MBraun M200B, $H_2O \leq 0.1 \, ppm$; $O_2 \leq 0.1 \, ppm$).

Synthesis of the Alkali Amidoboranes: The lithium and sodium amidoboranes were prepared by ball milling in a planetary ball miller (RETSCH PM100). All the reagents were handled inside the glove box.

An equimolar mixture of the metal hydride and AB was prepared in a stainless-steel reactor using 5 stainless-steel balls, which represent a ratio of 100 (weight of balls/reactants). To synthesize LiAB, $0.168 \times g$ of AB and $0.043 \times g$ of LiH were used. The reactor was transferred outside of the glove box and the mixture was milled for 5 h (four cycles of 1 h of milling at 400 rpm followed by a 15 min break). In the case of NaAB, $0.117 \times g$ of AB and $0.091 \times g$ of NaH were used. The mixture was milled for 10 min at 250 rpm. The difference on the milling cycles is explained by the higher reactivity of NaH toward AB in comparison with LiH.[63]

Once the milling was finished, the reactor was transferred back to the glove box and each one of the alkali amidoboranes was recovered and stored under inert atmosphere. The synthesis reactions for the amidoboranes were written as follows

$$NH_3BH_{3(s)} + LiH_{(s)} \rightarrow LiNH_2BH_{3(s)} + H_{2(g)} \tag{3}$$

$$NH_3BH_{3(s)} + NaH_{(s)} \rightarrow NaNH_2BH_{3(s)} + H_{2(g)} \tag{4}$$

Thermal Treatment: AB, LiAB, and NaAB were pyrolyzed at four different temperatures: 200, 600, 800, and 1000 °C. The pyrolysis at 200 °C was performed as a preliminary step to dehydropolymerize each one of these precursors, and to release most of the hydrogen carried by the molecules.

The as-obtained polymeric solids, used thus as preceramic polymers, were then pyrolyzed at higher temperatures to produce BN.

The pyrolysis at 200 °C was carried out in a stainless-steel reactor that was loaded with the sample inside the glove box and then transferred to the furnace. The heating ramp was as follows: the temperature was increased by 20 °C every 30 min, kept at 200 °C for 20 h, and then cooled down to room temperature. The reactor was put inside the glove box to recover the polymeric solid. In the case of the treatments at 600, 800, and 1000 °C, a tubular furnace was used. The sample was weighed and put into an alumina ceramic crucible inside the glove box, and transported into a sealed glass vessel under argon. The sample was introduced into the furnace, reducing the exposition to the air atmosphere to the minimum possible. The sample was then heated from room temperature to the targeted temperature at $1 \, °C \, min^{-1}$ under a N_2 atmosphere. After the pyrolysis, the obtained materials were recovered and stored inside the glove box. From here on, the samples were named ABX, LiABX, and NaABX, where $X = 200, 600, 800,$ or 1000 (which corresponded to the temperature of the heat treatment).

Characterization: The porosity of a selected group of the samples was investigated by N_2 adsorption technique with a Micromeritics TriFlex apparatus, using the Brunauer–Emmet–Teller method to calculate the specific surface area of the materials. Before the analysis, the samples were degassed overnight at 200 °C under a vacuum level of 1.33×10^{-3} mbar. All the samples were analyzed by Fourier-transform infrared spectroscopy (FTIR, NEXUS instrument, ThermoFisher, equipped with an attenuated total reflection accessory from 600 to $4000 \, cm^{-1}$ wavelength) and by magic-angle spinning nuclear magnetic resonance (MAS NMR, Varian VNMRS400 instrument, 400 MHz at 0 °C). All the materials were analyzed by ^{11}B MAS NMR while the samples derived from LiAB and NaB were also characterized by ^7Li and ^{23}Na MAS NMR, respectively. The samples were loaded into ZrO_2 rotors (3.2 mm diameter) inside the glove box. Raman spectroscopy analyses were carried out in a Horiba Yvon LabRAM instrument, equipped with a laser quantum gem 660 nm of 100 mW and an Olympus BX40 microscope. The materials analyzed by FTIR and Raman spectroscopy were put in a closed vial inside the glove box and transferred to the apparatus. Right before the analysis started, the samples were taken out of the vial and analyzed under air. The structure of the samples was analyzed by powder X-ray diffraction (PXRD) in a PANalytical X'pert Pro diffractometer with the Bragg–Brentano geometry, in the 20°–60° range of 2θ. The samples were prepared inside the glove box and protected from air with a Kapton film. X-ray photoelectron spectroscopy (XPS) analyses were performed in an ESCALAB 250 instrument (ThermoFisher) equipped with an Al–K_α monochromatized source of 1486.6 eV; the analysis was performed under air. Scanning electron microscopy and high-resolution transmission electron microscopy (SEM and HR-TEM) analyses were performed with a Hitachi S4800 and a JEOL 2200 FS (200 kV) microscopes, respectively. The samples were exposed to air previous the analyses.

Sorption of CO_2: The sorption of CO_2 of the samples was estimated using a Sievert system made in our laboratory. It was equipped with three pressure controllers (Keller PA-33X, range 0–3 bar, precision of ±1.5 mbar) and a temperature sensor (PT100 with a precision of ±0.15 °C at 30 °C). All the pipelines, valves, and connections were from Swagelok. To maintain a constant temperature during the experiment, the Sievert apparatus was enclosed in an incubation hood (Sartorius Certomat HK). Before the sorption experiments, the samples were degassed at 150 °C overnight. Right after, the samples were put in the measuring cell under argon (inside the glove box), transferred, and connected to the Sievert system. The measuring cell was degassed under vacuum for 5 h at 50 °C and then cooled down to 30 °C. Once all the variables were stable, the CO_2 was allowed to enter into the measuring cell with an initial pressure of 1.5 bar. The pressure and temperature were followed up during the process. The samples were left under CO_2 pressure until the equilibrium was achieved (within 180 min). The measurements were performed at least twice to assure the reproducibility of the results. The CO_2 was considered as an ideal gas to calculate the quantity adsorbed by the samples. Before the CO_2 sorption experiments, the density of the materials was estimated by helium pycnometry (Micromeritics AccuPycII 1340).

Supporting Information

Supporting Information is available from the Wiley Online Library or from the author.

Acknowledgements

Conflict of Interest

The authors declare no conflict of interest.

Data Availability Statement

The data that support the findings of this study are available on request from the corresponding author. The data are not publicly available due to privacy or ethical restrictions.

Keywords

[1] S. V. Anandhan, U. M. Krishnan, *Biomed. Mater.* **2021**, *16*, 044105.
[2] R. Han, F. Liu, X. Wang, M. Huang, W. Li, Y. Yamauchi, X. Sun, Z. Huang, *J. Mater. Chem. A* **2020**, *8*, 14384.
[3] G. R. Whittell, I. Manners, *Angew. Chem. Int. Ed.* **2011**, *50*, 10288.
[4] S. Frueh, R. Kellett, C. Mallery, T. Molter, W. S. Willis, C. King'Ondu, S. L. Suib, *Inorg. Chem.* **2011**, *50*, 783.
[5] Y. S. Chua, P. Chen, G. Wu, Z. Xiong, *Chem. Commun.* **2011**, *47*, 5116.
[6] R. Owarzany, P. J. Leszczyński, K. J. Fijalkowski, W. Grochala, *Crystals* **2016**, *6*, 88.
[7] S. Yuan, C. Journet, S. Linas, V. Garnier, P. Steyer, S. Benayoun, A. Brioude, B. Toury, *Crystals* **2016**, *6*, 55.
[8] E. M. M. Kumar, S. Sinthika, R. Thapa, *J. Mater. Chem. A* **2015**, *3*, 304.
[9] Y. Wang, F. Wang, B. Xu, J. Zhang, Q. Sun, Y. Jia, *J. Appl. Phys.* **2013**, *113*, 064309.
[10] H. Choi, Y. C. Park, Y. H. Kim, Y. S. Lee, *J. Am. Chem. Soc.* **2011**, *133*, 2084.
[11] Q. Sun, Z. Li, D. J. Searles, Y. Chen, G. Lu, A. Du, *J. Am. Chem. Soc.* **2013**, *135*, 8246.
[12] J. Dai, X. Wu, J. Yang, X. C. Zeng, *J. Phys. Chem. Lett.* **2014**, *5*, 393.
[13] J. Liang, Q. Song, J. Lin, G. Li, Y. Fang, Z. Guo, Y. Huang, C.-S. Lee, C. Tang, *ACS Sustainable Chem. Eng.* **2020**, *8*, 7454.
[14] J. F. Janik, W. C. Ackerman, R. T. Paine, D. W. Hua, A. Maskara, D. M. Smith, *Langmuir* **1994**, *10*, 514518.
[15] H. Jiang, L. Ma, Q. Yang, Z. Tang, X. Song, H. Zeng, C. Zhi, *Solid State Commun.* **2019**, *294*, 1.
[16] C. Yang, D. Liu, Y. Chen, C. Chen, J. Wang, Y. Fan, S. Huang, W. Lei, *ACS Appl. Mater. Interfaces* **2019**, *11*, 10276.
[17] F. Hojatisaeidi, M. Mureddu, F. Dessì, G. Durand, G. Durand, B. Saha, *Energies* **2020**, *13*, 549.

[18] K. Huang, L. Liang, S. Chai, U. Tumuluri, M. Li, Z. Wu, B. G. Sumpter, S. Dai, *J. Mater. Chem. A* **2017**, *5*, 16241.
[19] C. Yang, J. Wang, Y. Chen, D. Liu, S. Huang, W. Lei, *Nanoscale* **2018**, *10*, 10979.
[20] F. Xiao, Z. Chen, G. Casillas, C. Richardson, H. Li, Z. Huang, *Chem. Commun.* **2016**, *52*, 3911.
[21] J. Gou, C. Liu, J. Lin, C. Yu, Y. Fang, Z. Liu, Z. Guo, C. Tang, Y. Huang, *Ceram. Int.* **2022**, *48*, 11636.
[22] U. B. Demirci, *Int. J. Hydrog. Energy* **2017**, *42*, 9978.
[23] F. Toche, R. Chiriac, U. B. Demirci, P. Miele, *Int. J. Hydrog. Energy* **2012**, *37*, 6749.
[24] P. J. Fazen, E. E. Remsen, J. S. Beck, P. J. Carroll, A. R. McGhie, L. G. Sneddon, *Chem. Mater.* **1995**, *7*, 1942.
[25] J. Baumann, F. Baitalow, G. Wolf, *Thermochim. Acta* **2005**, *430*, 9.
[26] NIST, *National Institut of Standards and Technology*, US Department of Commerce, Boron Nitride, United States of America **2020**.
[27] K. J. Fijalkowski, R. Jurczakowski, W. Koźmiński, W. Grochala, *Phys. Chem. Chem. Phys.* **2012**, *14*, 5778.
[28] A. C. Stowe, W. J. Shaw, J. C. Linehan, B. Schmid, T. Autrey, *Phys. Chem. Chem. Phys.* **2007**, *9*, 1831.
[29] C. R. Miranda, G. Ceder, C. R. Miranda, G. Ceder, *J. Chem. Phys.* **2007**, *126*, 184703.
[30] D. Jacquemin, *J. Phys. Chem. A* **2004**, *108*, 9260.
[31] S. A. Shevlin, B. Kerkeni, Z. X. Guo, *Phys. Chem. Chem. Phys.* **2011**, *13*, 7649.
[32] J. Li, S. Bernard, V. Salles, C. Gervais, P. Miele, J. Li, *Chem. Mater.* **2010**, *22*, 2010.
[33] R. S. Chellappa, T. Autrey, M. Somayazulu, V. V. Struzhkin, R. J. Hemley, *ChemPhysChem* **2010**, *11*, 93.
[34] E. Magos-Palasyuk, A. Litwiniuk, T. Palasyuk, *Sci. Rep.* **2020**, *10*, article no. 17431.
[35] R. J. Nemanich, S. A. Solin, R. M. Martin, *Phys. Rev. B* **1981**, *23*, 6348.
[36] J. Wu, W. Q. Han, W. Walukiewicz, J. W. Ager, W. Shan, E. E. Haller, A. Zettl, *Nano Lett.* **2004**, *4*, 647.
[37] S. Yuan, B. Toury, C. Journet, A. Brioude, *Nanoscale* **2014**, *6*, 7838.
[38] S. Yuan, B. Toury, S. Benayoun, R. Chiriac, F. Gombault, C. Journet, A. Brioude, *Eur. J. Inorg. Chem.* **2014**, *2014*, 5507.
[39] J. B. Yang, J. Lamsal, Q. Cai, W. J. James, W. B. Yelon, *Appl. Phys. Lett.* **2008**, *92*, 091916.
[40] W. Lei, D. Liu, Y. Chen, *Adv. Mater. Interfaces* **2015**, *2*, 2.
[41] S. Alkoy, C. Toy, T. Gönül, A. Tekin, *J. Eur. Ceram. Soc.* **1997**, *17*, 1415.
[42] H. Yang, C. Iwamoto, T. Yoshida, *Thin Solid Films* **2005**, *483*, 218.
[43] J. Liu, X. Wang, S. Wu, Y. Li, Z. Jiang, L. Guo, X. Ye, *Int. J. Hydrog. Energy* **2020**, *45*, 2127.
[44] J. Zhang, Y. H. Hu, *Ind. Eng. Chem. Res.* **2011**, *50*, 8058.
[45] I. Milanović, N. Biliškov, *Int. J. Hydrog. Energy* **2020**, *45*, 7938.
[46] C. Koz, S. Acar, Y. Prots, P. Höhn, M. Somer, *Z. Anorg. Allg. Chem.* **2014**, *640*, 1.
[47] P. Bachmann, F. Düll, F. Späth, U. Bauer, H. P. Steinrück, C. Papp, *J. Chem. Phys.* **2018**, *149*, 164709.
[48] S. Yuan, S. Linas, C. Journet, P. Steyer, V. Garnier, G. Bonnefont, A. Brioude, B. Toury, *Sci. Rep.* **2016**, *6*, article no. 20388.
[49] D. Schild, S. Ulrich, J. Ye, M. Stüber, *Solid State Sci.* **2010**, *12*, 1903.
[50] N. Badi, *J. Adv. Dielectr.* **2015**, *5*, 1550029.
[51] M. S. Bresnehan, M. J. Hollander, M. Wetherington, K. Wang, T. Miyagi, G. Pastir, D. W. Snyder, J. J. Gengler, A. A. Voevodin, W. C. Mitchel, J. A. Robinson, *J. Mater. Res.* **2014**, *29*, 459.
[52] X. Gouin, P. Grange, L. Bois, P. L'Haridon, Y. Laurent, *J. Alloys Compd.* **1995**, *224*, 22.
[53] J. I. Oñate, A. García, V. Bellido, J. L. Viviente, *Surf. Coat. Technol.* **1991**, *49*, 548.
[54] D. N. Hendrickson, J. M. Hollander, W. L. Jolly, *Inorg. Chem.* **1970**, *9*, 612.

**ADVANCED
SCIENCE NEWS**

www.advancedsciencenews.com

Energy Technology
Generation, Conversion, Storage, Distribution

www.entechnol.de

[55] A. V. Naumkin, A. Kraust-Vass, S. W. Gaarenstroom, C. J. Powell, *NIST XPS Database*, United States of America **2020**.

[56] A. Tokarev, E. Kjeang, M. Cannon, D. Bessarabov, *Int. J. Hydrog. Energy* **2016**, *41*, 16984.

[57] F. Shayeganfar, R. Shahsavari, *Langmuir* **2016**, *32*, 13313.

[58] Y. Wang, Z. X. Guo, *J. Mater. Chem. A* **2014**, *2*, 6801.

[59] Z. Xiong, G. Wu, J. Hu, Y. Liu, P. Chen, W. Luo, J. Wang, *Adv. Funct. Mater.* **2007**, *17*, 1137.

[60] N. K. Singh, T. Kobayashi, O. Dolotko, J. W. Wiench, M. Pruski, V. K. Pecharsky, *J. Alloys Compd.* **2012**, *513*, 324.

[61] K. J. Fijałkowski, W. Grochala, *J. Mater. Chem.* **2009**, *19*, 2043.

[62] K. Shimoda, Y. Zhang, T. Ichikawa, H. Miyaoka, Y. Kojima, *J. Mater. Chem.* **2011**, *21*, 2609.

[63] Z. Xiong, C. K. Yong, G. Wu, P. Chen, W. Shaw, A. Karkamkar, T. Autrey, M. O. Jones, S. R. Johnson, P. P. Edwards, W. I. F. David, *Nat. Mater.* **2008**, *7*, 138.